Incomplete erasure of histone marks during epigenetic reprogramming in medaka early development

Authors/Affiliations

Hiroto S. Fukushima[1], Hiroyuki Takeda[1] and Ryohei Nakamura[1]

[1]Department of Biological Sciences, Graduate School of Science, The University of Tokyo, Tokyo, 113-0033, Japan

Correspondence to: htakeda@bs.s.u-tokyo.ac.jp, rynakamura@bs.s.u-tokyo.ac.jp

Supplementary Figures

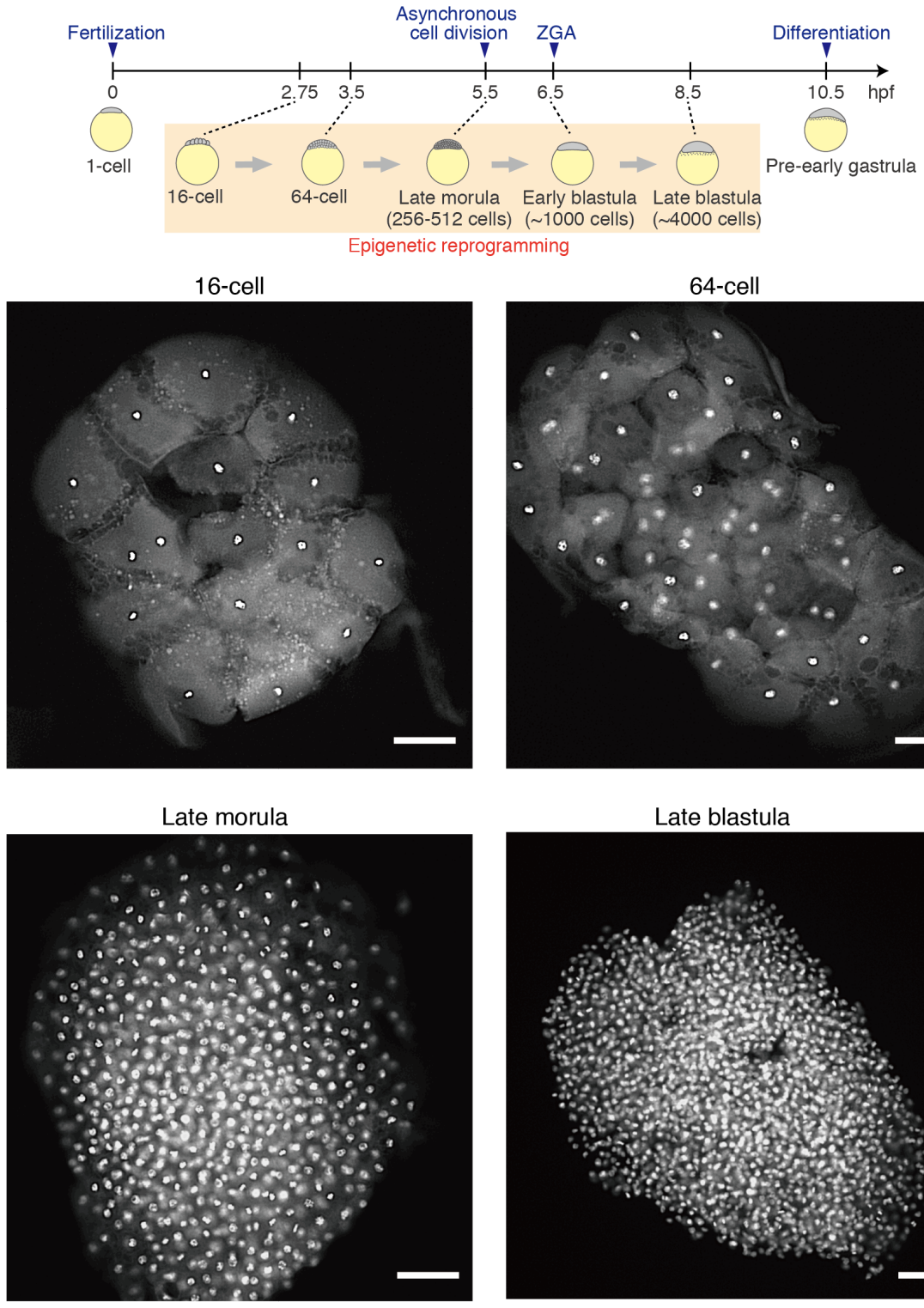

Supplemental Figure S1. Medaka development
A schematic of medaka development and blastoderms after DAPI-staining at the four stages that we mainly focused on in this study. Scale bars indicate 100 μm.

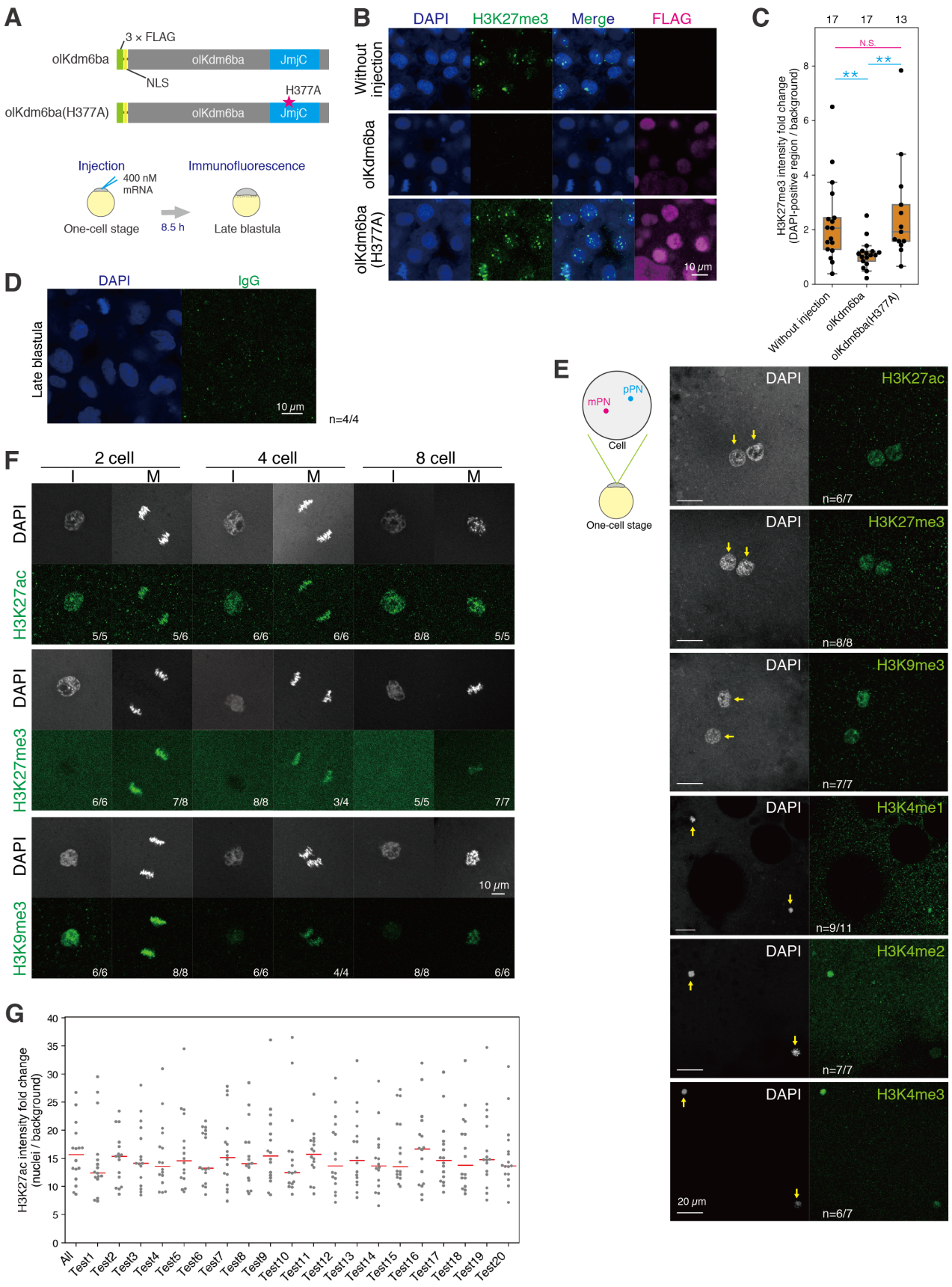
A
3 × FLAG
olKdm6ba
olKdm6ba
JmjC
NLS
H377A
olKdm6ba(H377A)
olKdm6ba
JmjC
Injection
400 nM mRNA
Immunofluorescence
One-cell stage
8.5 h
Late blastula
B
DAPI
H3K27me3
Merge
FLAG
Without injection
olKdm6ba
olKdm6ba (H377A)
10 μm
C
17
17
13
N.S.
**
**
H3K27me3 intensity fold change (DAPI-positive region / background)
0
2
4
6
8
Without injection
olKdm6ba
olKdm6ba(H377A)
D
DAPI
IgG
Late blastula
10 μm
n=4/4
E
mPN
pPN
Cell
One-cell stage
DAPI
H3K27ac
n=6/7
DAPI
H3K27me3
n=8/8
DAPI
H3K9me3
n=7/7
DAPI
H3K4me1
n=9/11
DAPI
H3K4me2
n=7/7
DAPI
H3K4me3
20 μm
n=6/7
F
2 cell
4 cell
8 cell
I
M
I
M
I
M
DAPI
H3K27ac
5/5
5/6
6/6
6/6
8/8
5/5
DAPI
H3K27me3
6/6
7/8
8/8
3/4
5/5
7/7
DAPI
H3K9me3
10 μm
6/6
8/8
6/6
4/4
8/8
6/6
G
H3K27ac intensity fold change (nuclei / background)
0
5
10
15
20
25
30
35
40
All
Test1
Test2
Test3
Test4
Test5
Test6
Test7
Test8
Test9
Test10
Test11
Test12
Test13
Test14
Test15
Test16
Test17
Test18
Test19
Test20

Supplemental Figure S2. Supporting data for Figure 1
(A) Schematics of constructs (wildtype olKdm6ba and its catalytically inactive point mutant olKdm6ba(H377A)) and experimental design.
(B) Immunofluorescence staining at the late blastula stage showing depletion of H3K27me3 by olKdm6ba injection.
(C) Boxplots showing the signal intensities of each histone modification in DAPI-positive regions. Each dot indicates the average intensity in a single embryo. The intensity was normalized by background intensity. The number above each plot indicates the number of embryos examined. Dwass, Steel, Critchlow and Fligner all-pairs comparison test, *** $p < 0.001$, ** $p < 0.01$, * $p < 0.05$, respectively.
(D) Immunofluorescence staining using IgG at the late blastula stage.
(E) Immunofluorescence staining of histone modifications at the one-cell stage. Yellow arrows indicate either paternal (pPN) or maternal pronuclei (mPN) in one-cell stage embryos. The fraction of embryos with the representative pattern was indicated at the bottom.
(F) Immunofluorescence staining of histone modifications at the two-cell, four-cell and eight-cell stage. I and M indicate interphase and mitotic phase, respectively. The fraction of embryos with the representative pattern was indicated at the bottom.
(G) Swarm plot indicates signal intensities measured using all nuclei without down-sampling (All) or using randomly chosen four nuclei (Test1-20). Red bars indicate medians of dots. Random down-sampling was repeated for twenty times, but we could not find large difference between the data with and without down-sampling.

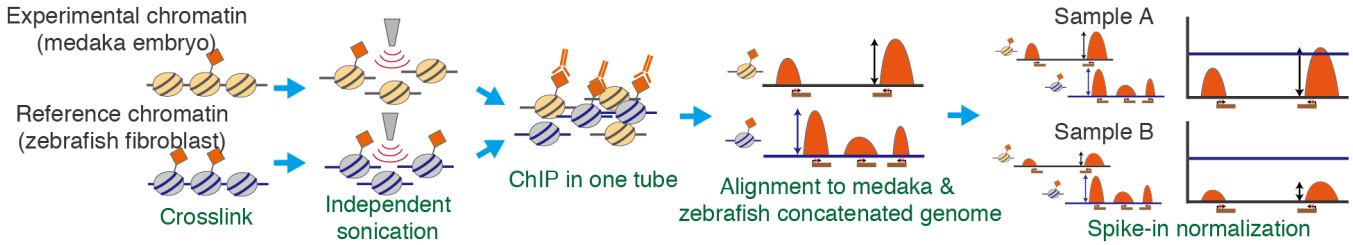

Supplemental Figure S3. A schematic illustration of spike-in ChIP-seq method used in this study
We prepared reference chromatin from a zebrafish fibroblast cell line (BRF41) and mixed it with experimental chromatin (medaka embryo chromatin) in the same tube, which was then subjected to ChIP-seq. All reads were aligned to the medaka and zebrafish concatenated genome. Theoretically, the enrichment level of modifications in reference chromatin should be the same for all samples, so the level of histone modifications in experimental chromatin were normalized using the reference chromatin ChIP signal.

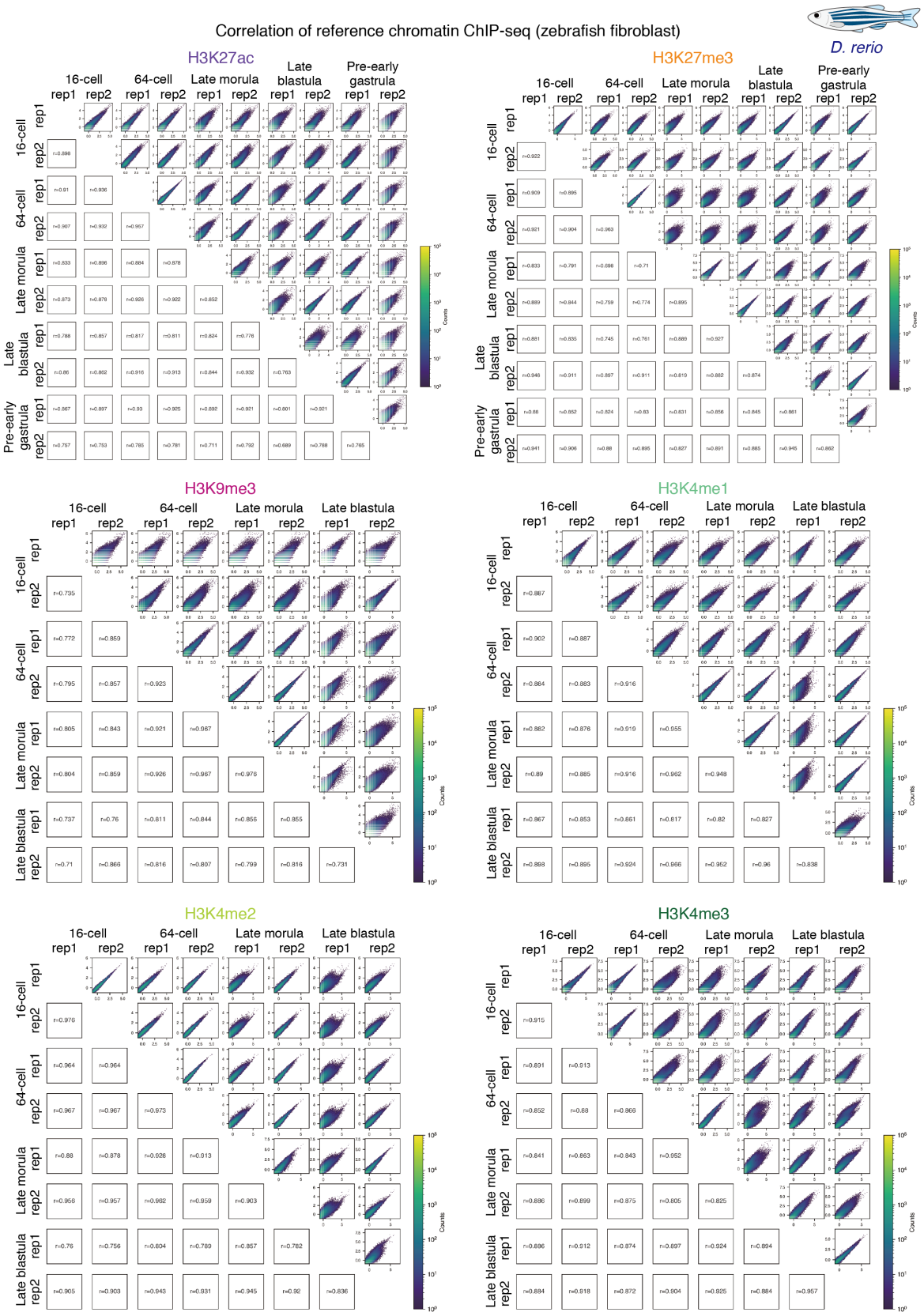

Supplemental Figure S4. Reproducibility of histone modification enrichment in reference chromatin (zebrafish fibroblast) revealed by spike-in ChIP-seq
2D histograms showing correlation between each reference chromatin. Log2 (RPKMconv + 0.5) for each 5000 bp window-divided genomic interval and Pearson's correlation coefficients (r) are shown (RPKMconv: conventional RPKM).

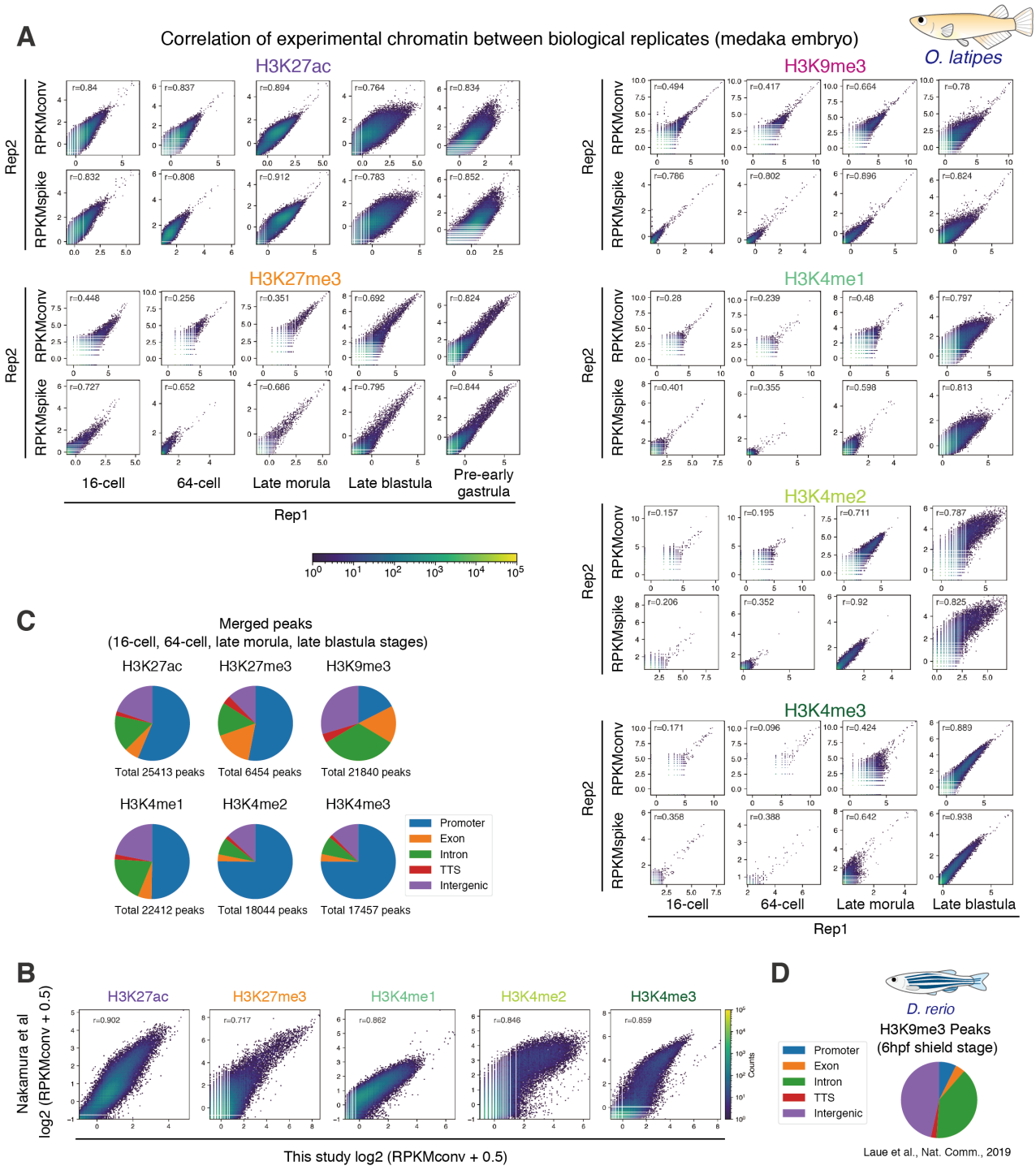

Supplemental Figure S5. Reproducibility of histone modification enrichment in experimental chromatin (medaka embryo) revealed by spike-in ChIP-seq

(A) 2D histograms showing correlation between two biological replicates of experimental chromatin. Log2 (RPKMconv or RPKMspike + 0.5) for each 5000 bp window-divided genomic interval and Pearson's correlation coefficients (r) are shown (RPKMconv: conventional RPKM, RPKMspike: spike-in normalized RPKM).

(B) 2D histogram showing correlation between ChIP-seq data in this study and that in a previous study (Nakamura et al. 2014).

(C) Pie charts showing genomic distribution of spike-in ChIP-seq peaks for each modification. Peaks from the four developmental stages (the 16-cell, 64-cell, late morula and late blastula stage) were merged (see Method) and used.

(D) Pie chart showing genomic distribution of H3K9me3 ChIP-seq peaks in a previous zebrafish study (Laue et al. 2019).

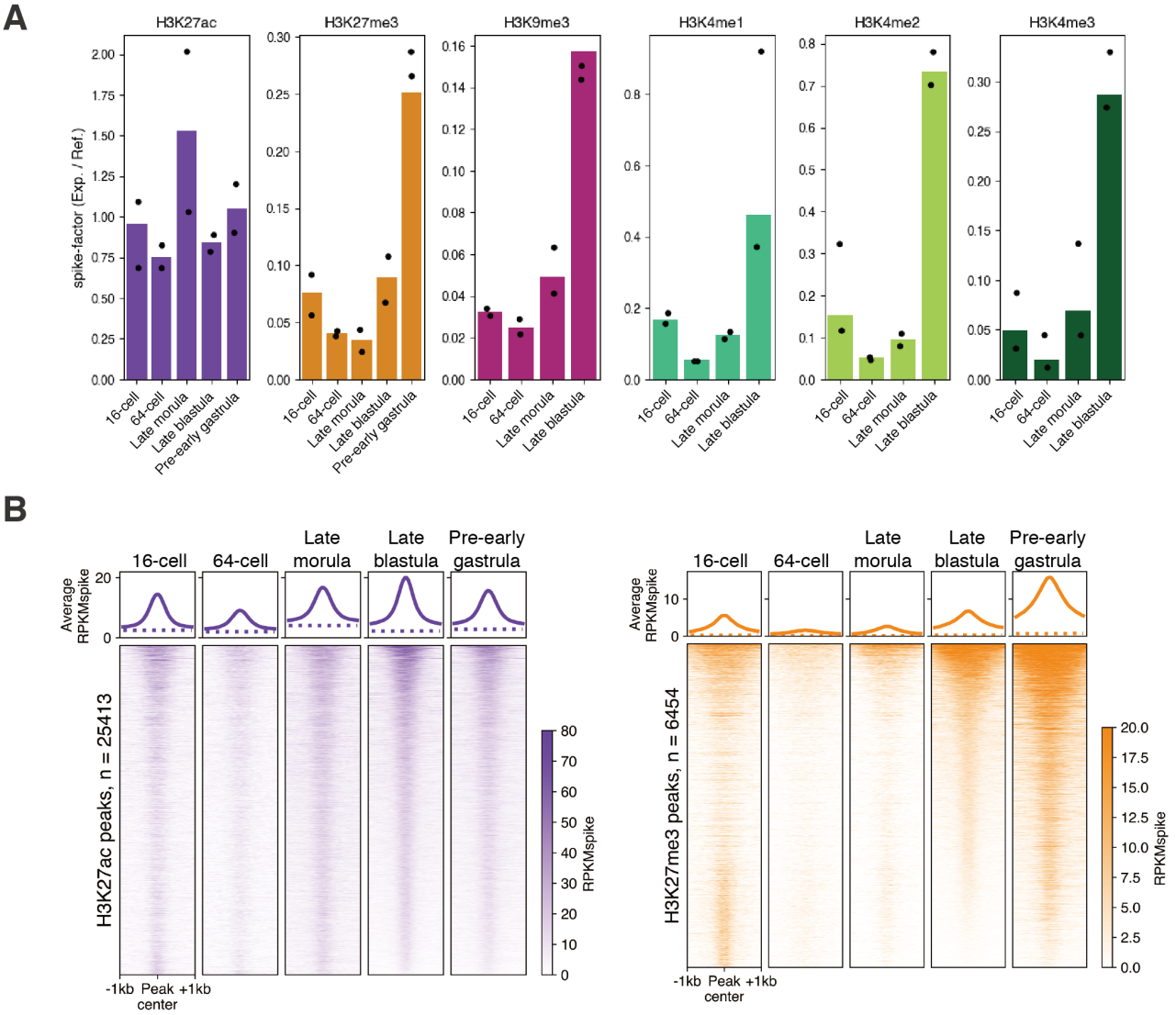

Supplemental Figure S6. Global level of each modification after spike-in normalization
(A) Bar plots showing the global level of each modification at all stages calculated by spike-in ChIP-seq (see method for details). Here, bars and dots indicate values of pooled samples and individual replicates, respectively. We note that the values of pooled samples (bars) are not just the average of two replicates (dots) because deduplication affects the number of total reads.
(B) Genome-wide changes in enrichment of each modification including the pre-early gastrula stage data (also refer to Figure 2B). The average enrichment levels after spike-in normalization (RPKMspike) around all peaks and randomized peaks at each stage are shown as solid lines and dashed lines, respectively (top). Heatmaps showing enrichment levels (RPKMspike) around all peaks (± 1 kb from peak center).

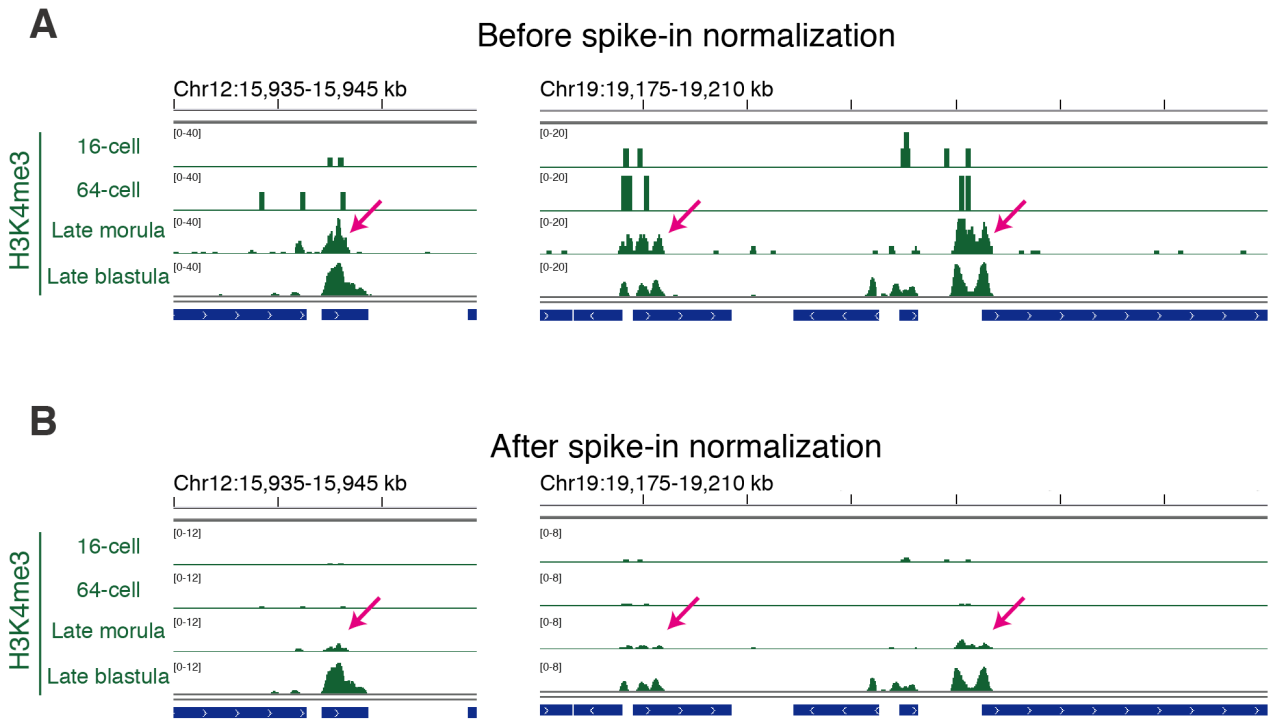

Supplemental Figure S7. Spike-in normalization revealed very limited accumulation of H3K4me3 at the late morula stage
(A-B) Track views showing H3K4me3 enrichment before (A) and after spike-in normalization (B). Arrows indicate the genomic regions where H3K4me3 accumulation is observed before spike-in normalization.

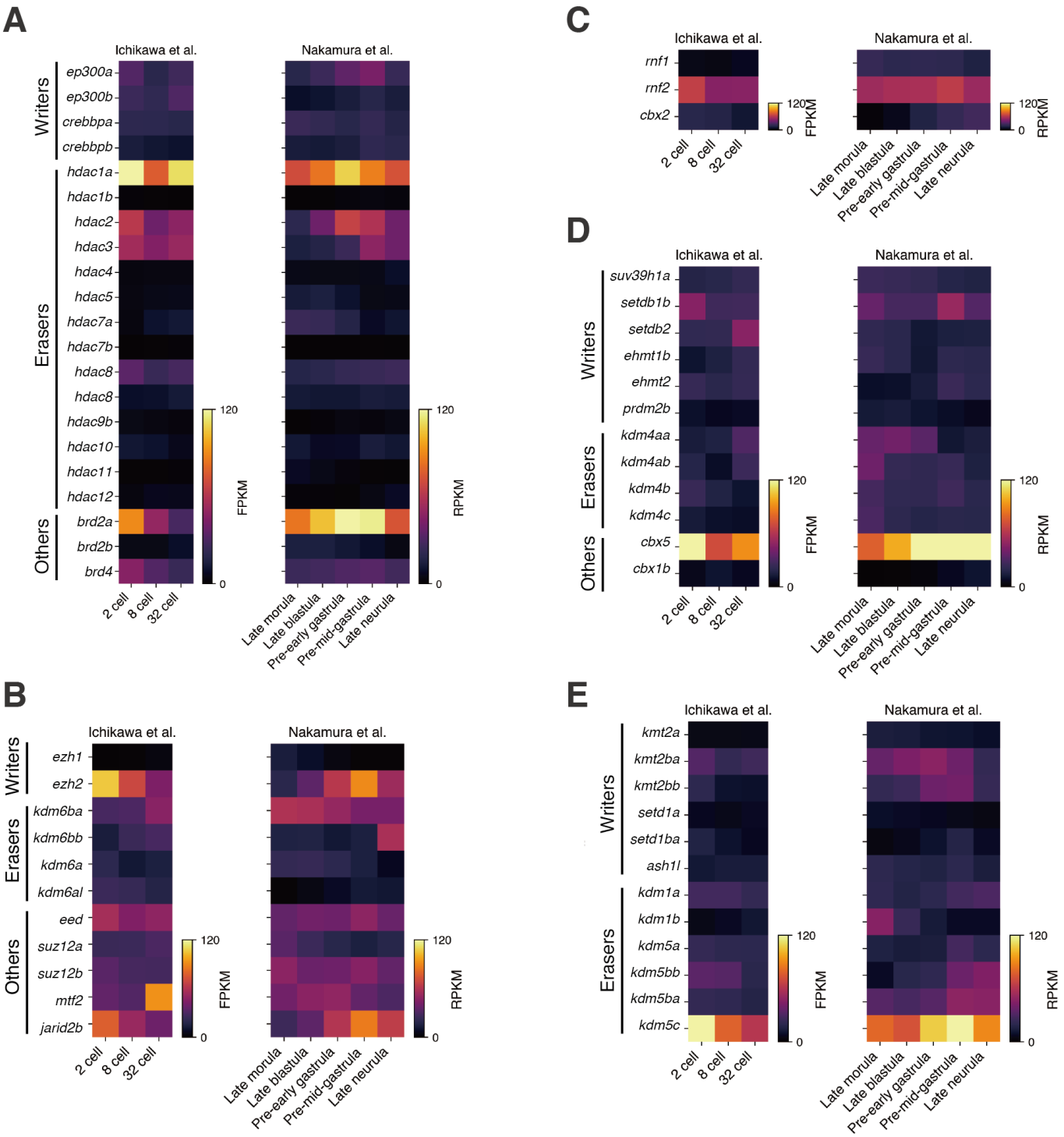

Supplemental Figure S8. Expression levels of writers, erasers and other related proteins of histone modifications
(A) Expression levels of writers, erasers and readers of H3K27ac.
(B) Expression levels of writers, erasers and PRC2 components, related to H3K27me3.
(C) Expression level of PRC1 components, related to H3K27me3.
(D) Expression levels of writers, erasers and readers of H3K9me3.
(E) Expression levels of writers, erasers of H3K4 methylations.
RNA-seq data of the 2-cell, 8-cell and 32-cell stages were obtained from (Ichikawa et al. 2017) and the late morula, late blastula and pre-early gastrula stages were obtained from (Nakamura et al. 2021).

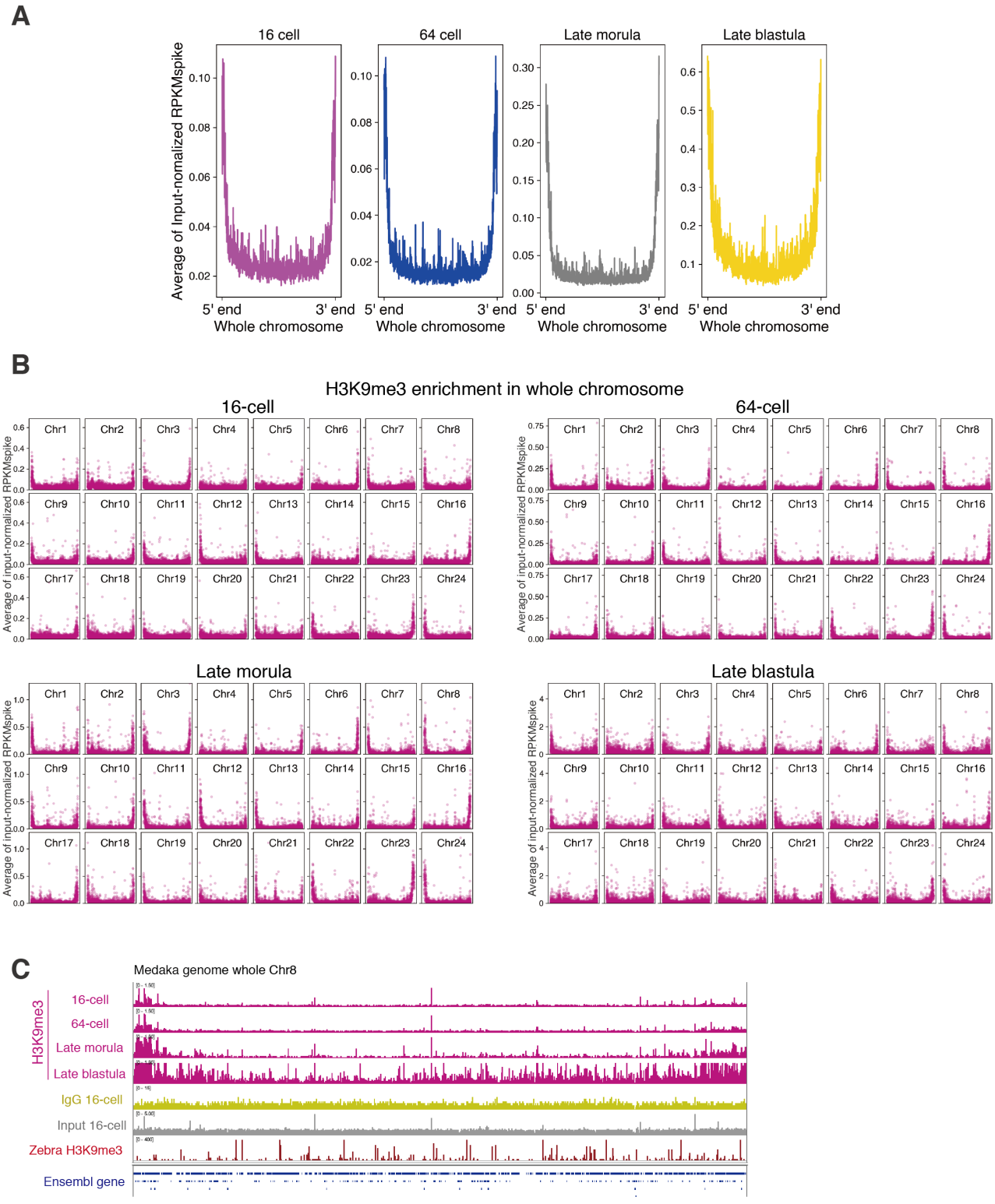

Supplemental Figure S9. Spike-in ChIP-seq showing retention of H3K9me3 localized at telomeric regions.
(A) Average H3K9me3 signals of all chromosomes at four stages after spike-in normalization. The data in at each stage are shown separately here. To exclude repeat bias, the signal was further normalized by input signal (see Method).
(B) H3K9me3 enrichment along all individual chromosomes at four stages after spike-in normalization. Each dot represents input-normalized RPKMspike levels within 10 kb-divided genomic intervals.
(C) Track view showing zebrafish H3K9me3 ChIP-seq reads (Laue et al. 2019) aligned to medaka genome (Zebra H3K9me3) and medaka ChIP-seq (H3K9me3, IgG and input).

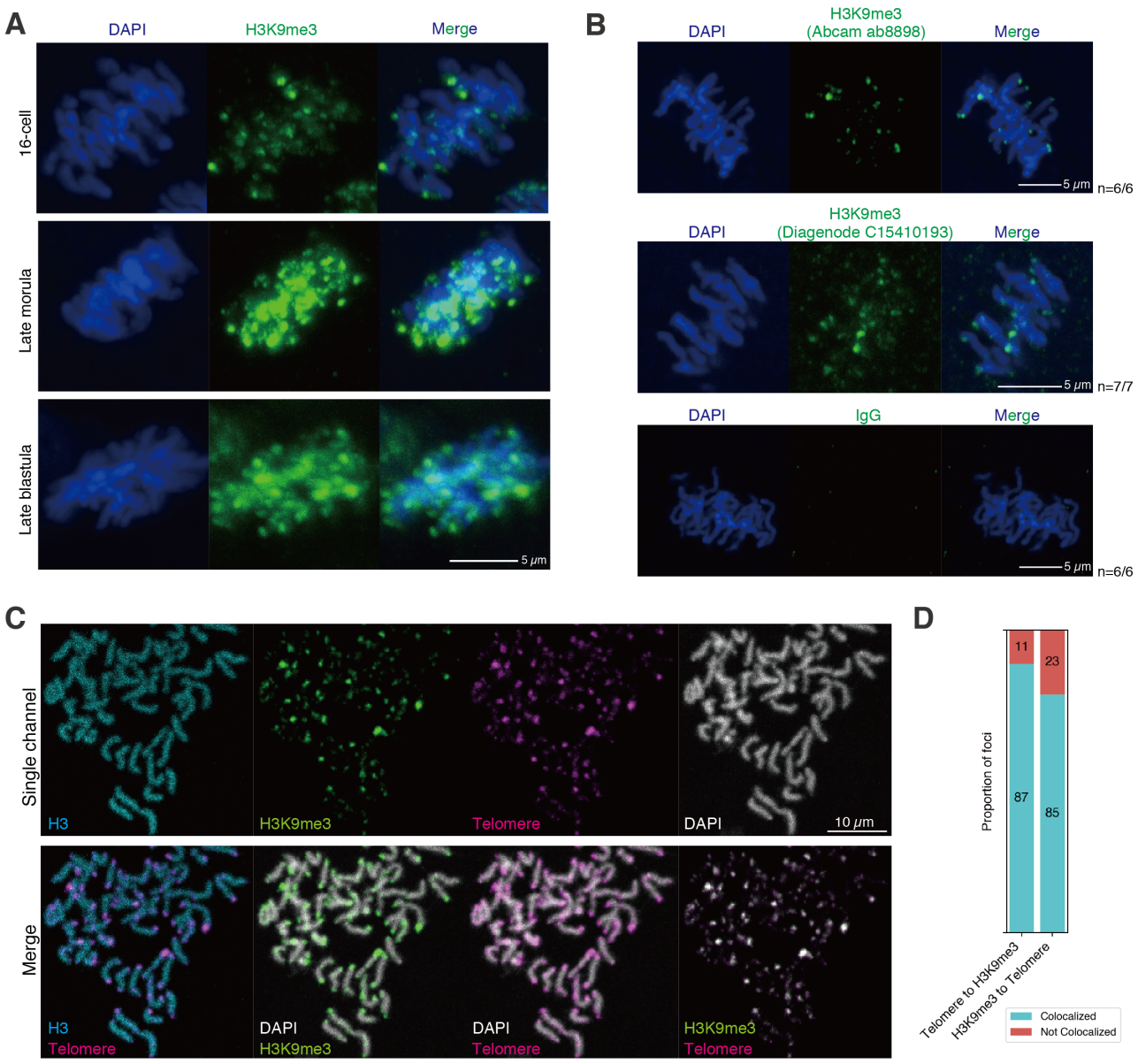

Supplemental Figure S10. Imaging data showing retention of H3K9me3 at telomeric regions.
(A) Immunofluorescence staining of H3K9me3 in mitotic phase (metaphase or anaphase). See also Figure 3C (data at the 64-cell stage).
(B) Immunofluorescence staining of H3K9me3 (using two different antibodies) and IgG in mitotic phase at the 64-cell stage showing specific signals at chromosome ends and absence of signals, respectively.
(C) FISH and immunofluorescence staining using chromosome spreads from embryos at the 64-cell stage.
(D) The proportion of colocalized foci in Supplemental Fig. S10C. For example, the blue bar in “Telomere to H3K9me3” indicates the proportion of telomere foci colocalizing with H3K9me3 foci. The numbers in bars indicate numbers of the foci.

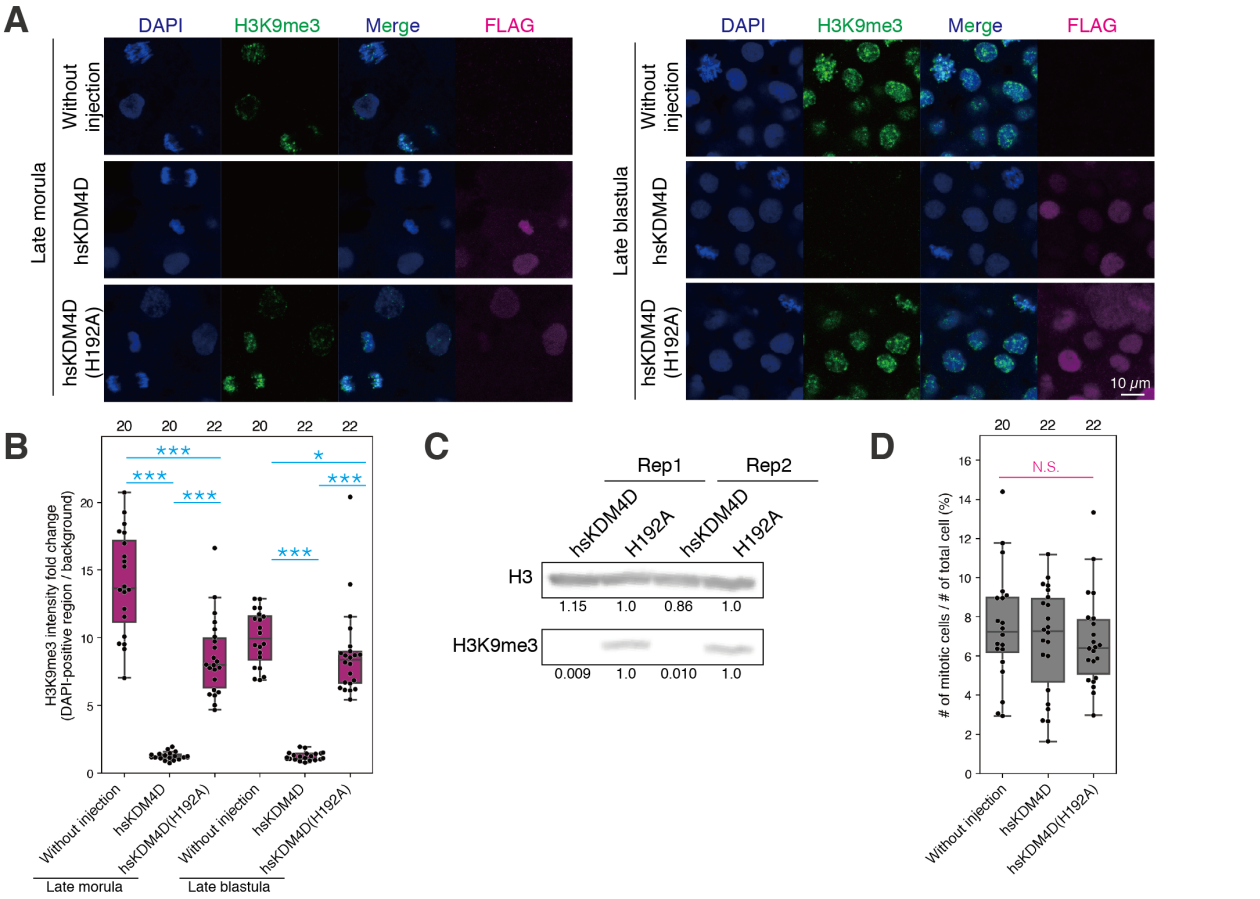
A
DAPI
H3K9me3
Merge
FLAG
Late morula
Late blastula
Without injection
hsKDM4D
hsKDM4D (H192A)
10 μm
B
H3K9me3 intensity fold change (DAPI-positive region / background)
Without injection
hsKDM4D
hsKDM4D(H192A)
Late morula
Late blastula
C
Rep1
Rep2
H3
H3K9me3
1.15
1.0
0.86
1.0
0.009
1.0
0.010
1.0
D
# of mitotic cells / # of total cell (%)
N.S.
E
Without injection
hsKDM4D
hsKDM4D(H192A)
1 dpi
3 dpi
F
Rep1
Rep2
Proportion of embryos (%)
8 hpi (Late blastula)
1 dpi (Early-late neurula)
3 dpi (34-35 somite)
Normal
Abnormal
Delay
Dead
G
Misaligned chromosomes
Prophase
Anaphase
5 μm

Supplemental Figure S11. Supporting data for hsKDM4D experiments
(A) Immunofluorescence staining of H3K9me3 and FLAG.
(B) Boxplots showing the signal intensities of each histone modification in DAPI-positive regions. Each dot indicates the average intensity in a single embryo. FLAG signal indicates the enrichment level of translated hsKDM4D proteins. The intensity was normalized by background intensity. Phases of the cell cycle after the late morula stage are not indicated because cells divide asynchronously from the late morula stage. See also Figure 4A (schematics of experiments) and 4B (data at the 64-cell stage). The number above each plot indicates the number of embryos examined. Dwass, Steel, Critchlow and Fligner all-pairs comparison test, *** $p < 0.001$, ** $p < 0.01$, * $p < 0.05$, respectively.
(C) Western blot showing global reduction in H3K9me3 by hsKDM4D injection at the late blastula stage. Samples from nineteen hsKDM4D-injected or hsKDM4D(H192A)-injected embryos were loaded to each lane. Numbers indicate signals normalized to hsKDM4D(H192A)-injected samples in each replicate.
(D) Boxplots showing the fraction of mitotic cells in control (without injection), hsKDM4D-injected, or hsKDM4D(H192A)-injected late blastula embryos. The number above each plot indicates the number of embryos examined. Tukey-Kramer test, not significant (N.S.).
(E) Phenotypes of embryos injected with hsKDM4D.
(F) Percentages of embryos showing each phenotype. Two biological replicates are shown separately. The number above each bar indicates the total number of embryos in each condition. hpi/dpi = hours/days post injection.
(G) Representative phenotypes of chromosome segregation errors (misaligned chromosomes). Arrows indicate the errors. See also Figure 4C, 4D.

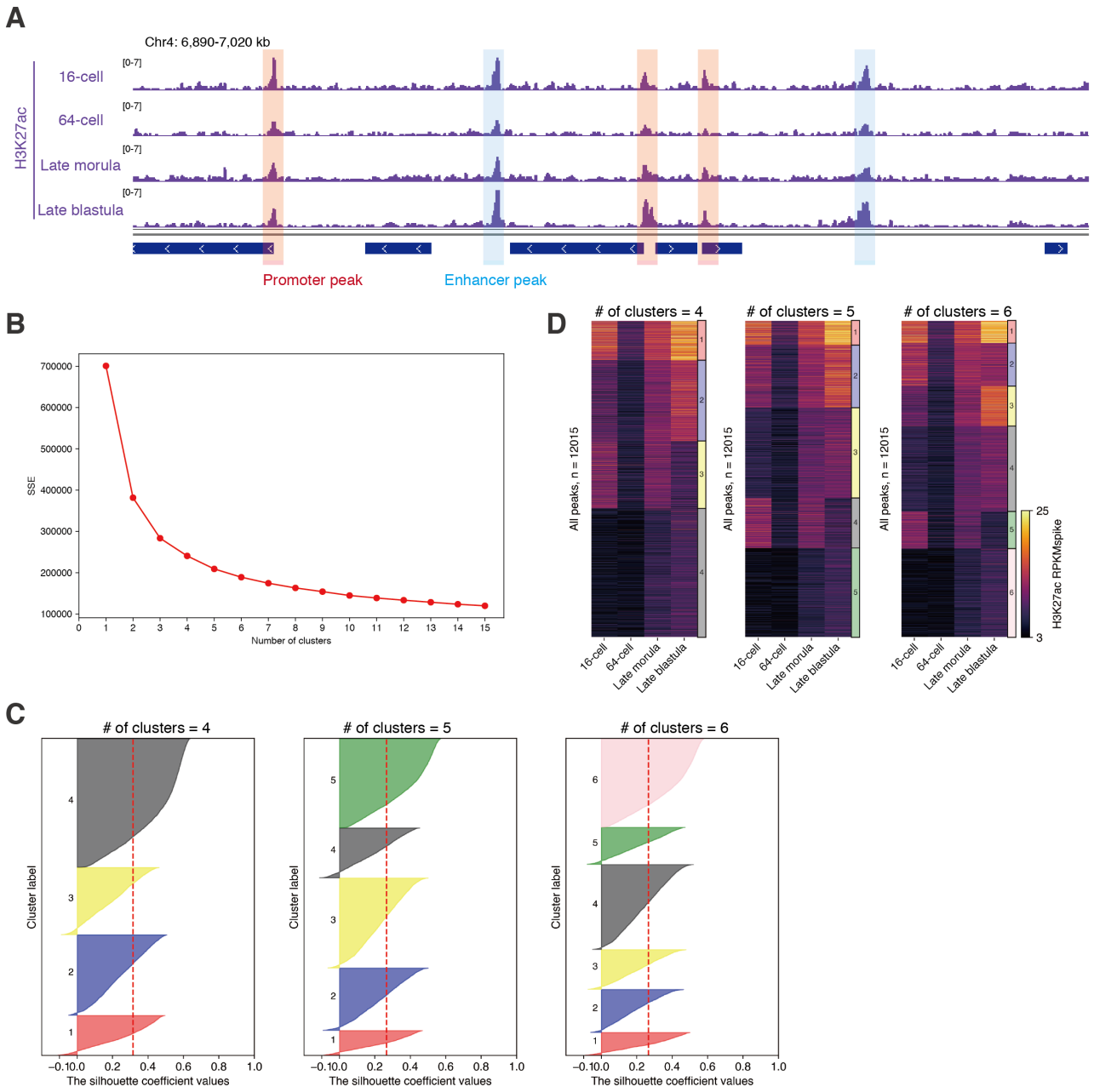

Supplemental Figure S12. Decision of number of clusters for k-means clustering of H3K27ac-marked promoters.
(A) Track view showing promoter peaks (peaks within -2.5 kb ≤ TSS ≤ 2.5 kb, red) and enhancer peaks (peaks at least 2 kb away from promoter peaks, blue) of H3K27ac.
(B) Elbow method for the decision of optimal cluster number for k-means. Line plot showing sum of squared errors (SSE) after k-means clustering titrating the number of clusters. This analysis showed that the SSE starts decreasing in an almost linear fashion from cluster number = 5, suggesting that the optimal number of clusters is around 5.
(C) Silhouette analysis for the deciding of optimal cluster number for k-means. Horizontal bar plots showing the silhouette coefficient value in each element, and dashed line indicates the average silhouette coefficient. Ideally, each cluster should show as many as possible elements with a higher silhouette coefficient. From this perspective, we concluded that cluster number 5 or 6 is better than 4.
(D) A heatmap showing H3K27ac enrichment in H3K27ac-marked promoters after k-means clustering using different cluster numbers. Based on the results of Supplemental Figure S12A, the heatmaps using k = 4, 5 or 6 were compared. However, the cluster showed similar characters between those heatmaps. Therefore, we concluded that the best number of clusters for k-means was 5.

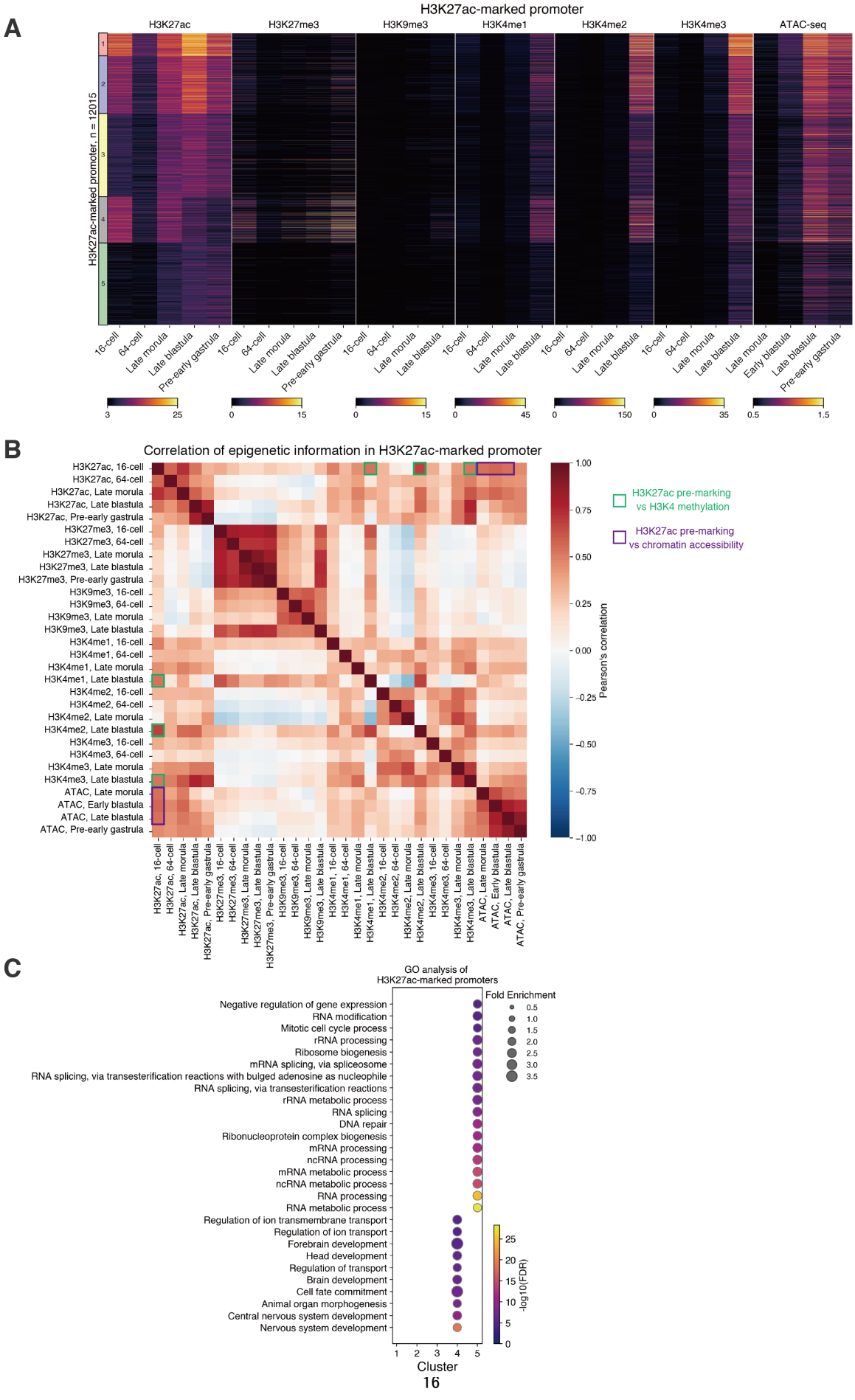
A
H3K27ac-marked promoter
H3K27ac
H3K27me3
H3K9me3
H3K4me1
H3K4me2
H3K4me3
ATAC-seq
H3K27ac-marked promoter, n = 12015
16-cell
64-cell
Late morula
Late blastula
Pre-early gastrula
Early blastula
B
Correlation of epigenetic information in H3K27ac-marked promoter
Pearson's correlation
H3K27ac pre-marking vs H3K4 methylation
H3K27ac pre-marking vs chromatin accessibility
C
GO analysis of H3K27ac-marked promoters
Fold Enrichment
Negative regulation of gene expression
RNA modification
Mitotic cell cycle process
rRNA processing
Ribosome biogenesis
mRNA splicing, via spliceosome
RNA splicing, via transesterification reactions with bulged adenosine as nucleophile
RNA splicing, via transesterification reactions
rRNA metabolic process
RNA splicing
DNA repair
Ribonucleoprotein complex biogenesis
mRNA processing
ncRNA processing
mRNA metabolic process
ncRNA metabolic process
RNA processing
RNA metabolic process
Regulation of ion transmembrane transport
Regulation of ion transport
Forebrain development
Head development
Regulation of transport
Brain development
Cell fate commitment
Animal organ morphogenesis
Central nervous system development
Nervous system development
-log10(FDR)
Cluster

Supplemental Figure S13. Characters of H3K27ac-marked promoters.
(A) Heatmaps showing epigenetic modification levels at H3K27ac-marked promoters.
(B) A heatmap showing Pearson's correlation of epigenetic information in H3K27ac-marked promoters.
(C) GO terms (biological process) enriched in the genes associated with each H3K27ac-marked promoter cluster. Only those GO terms (biological process) which have an FDR less than 10^{-5} and whose enrichment more than 2.1 fold were listed. Color indicates FDR, and circle size is the fold enrichment of each GO term.

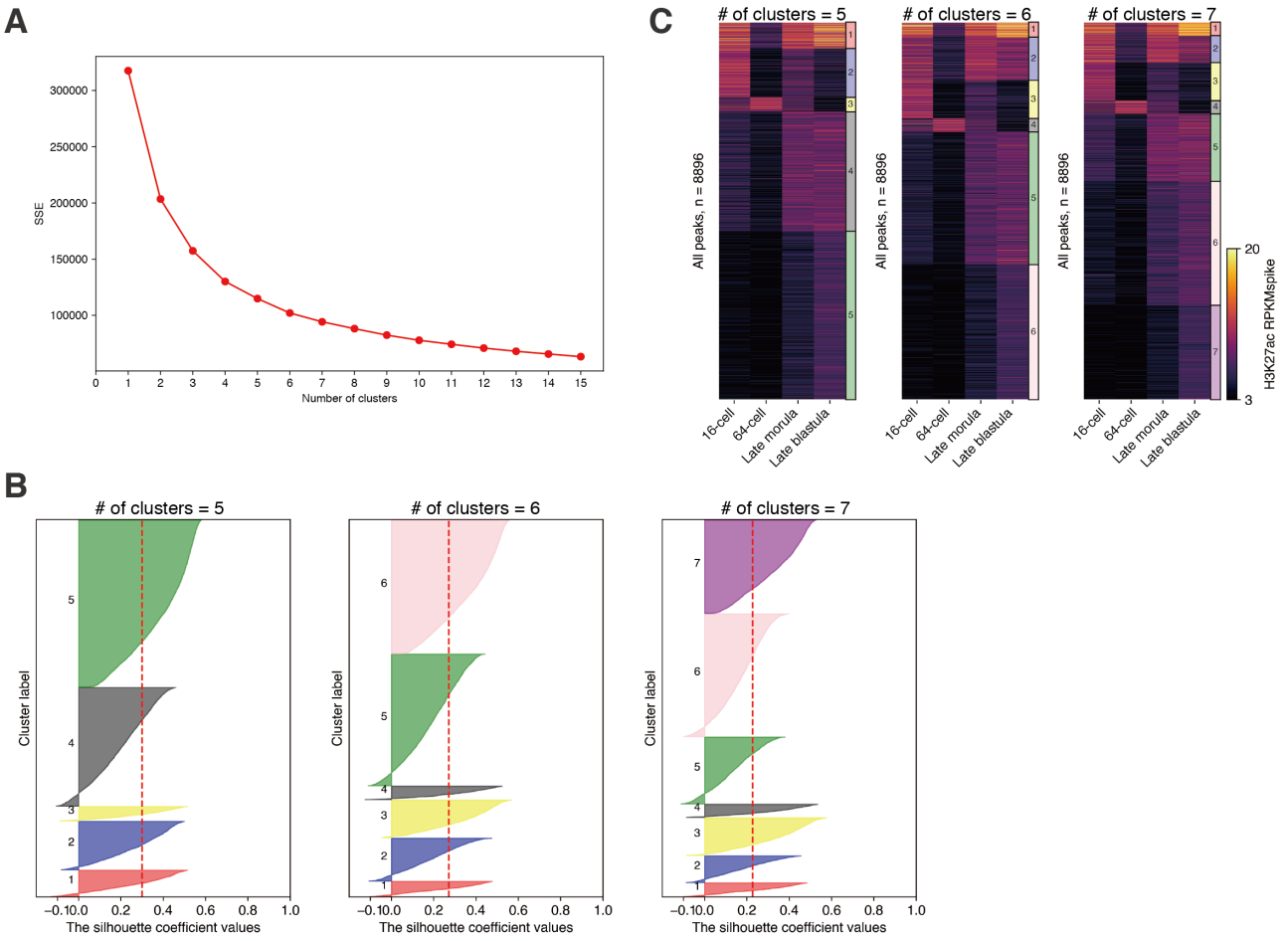

Supplemental Figure S14. Decision of number of clusters for k-means clustering of H3K27ac-marked enhancers.
(A) Elbow method for the decision of optimal cluster number for k-means. Line plot showing sum of squared errors (SSE) after k-means clustering titrating the number of clusters. From this, the SSE starts decreasing in an almost linear fashion from cluster number = 6, suggesting that the optimal number of clusters is around 6.
(B) Silhouette analysis for deciding of optimal cluster number for k-means. Horizontal bar plots showing silhouette coefficient value in each element, and dashed line indicating the average silhouette coefficient. Ideally, each cluster should show as many as possible elements with higher silhouette coefficient. From this perspective, we concluded that cluster number 6 is optimal.
(C) Heatmaps showing H3K27ac enrichment in H3K27ac-marked promoters after k-means clustering using different cluster numbers. Based on the results of Supplemental Figure S14A, the heatmaps using several numbers of clusters = 5, 6 or 7 were compared. Given that the cluster having very different character was not found among those heatmaps, we concluded that the best number of clusters for k-means was 6.

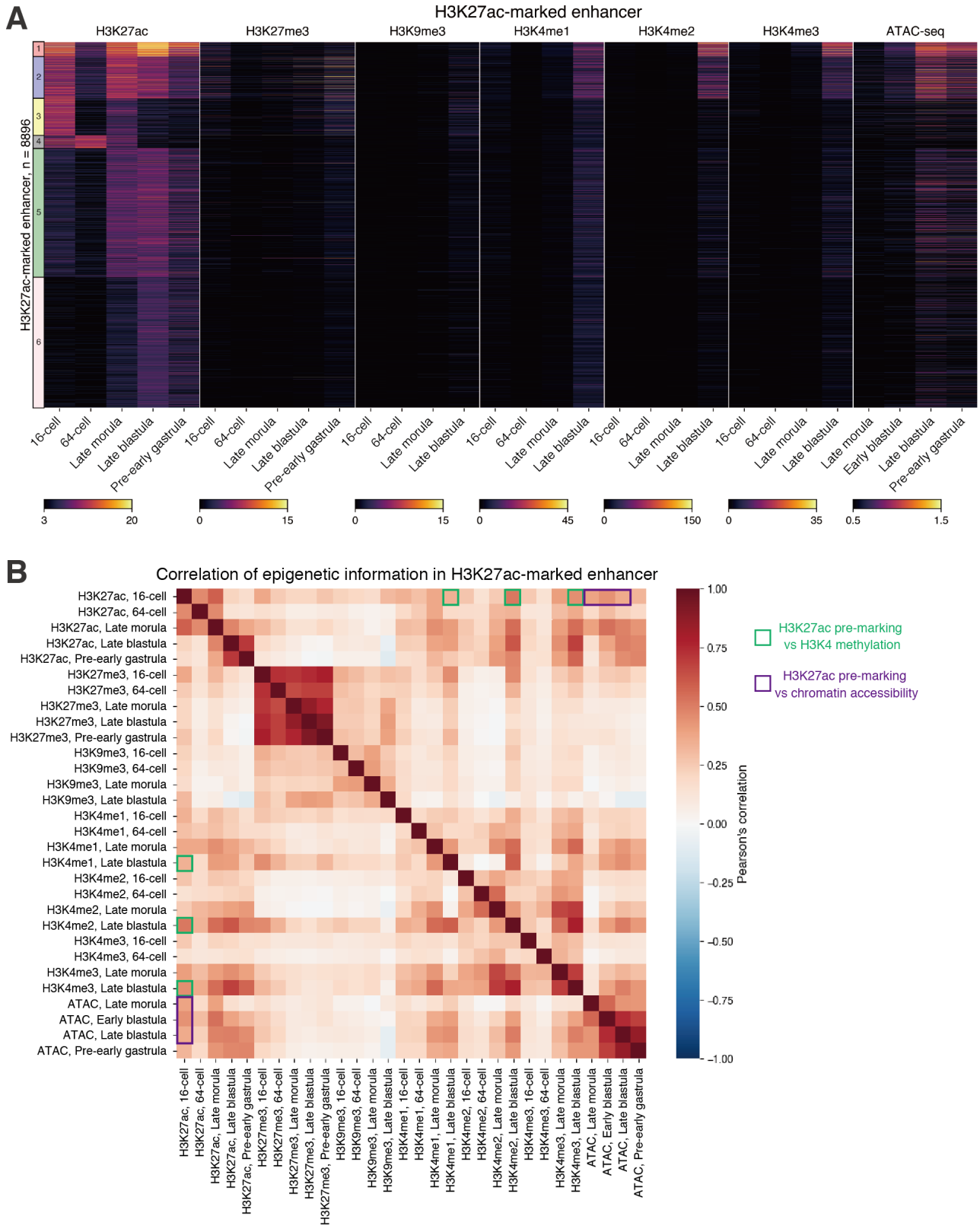

Supplemental Figure S15. Characters of H3K27ac-marked enhancers
(A) A heatmap showing epigenetic modifications of H3K27ac-marked enhancers.
(B) A heatmap showing Pearson's correlation of epigenetic information in H3K27ac-marked enhancers.

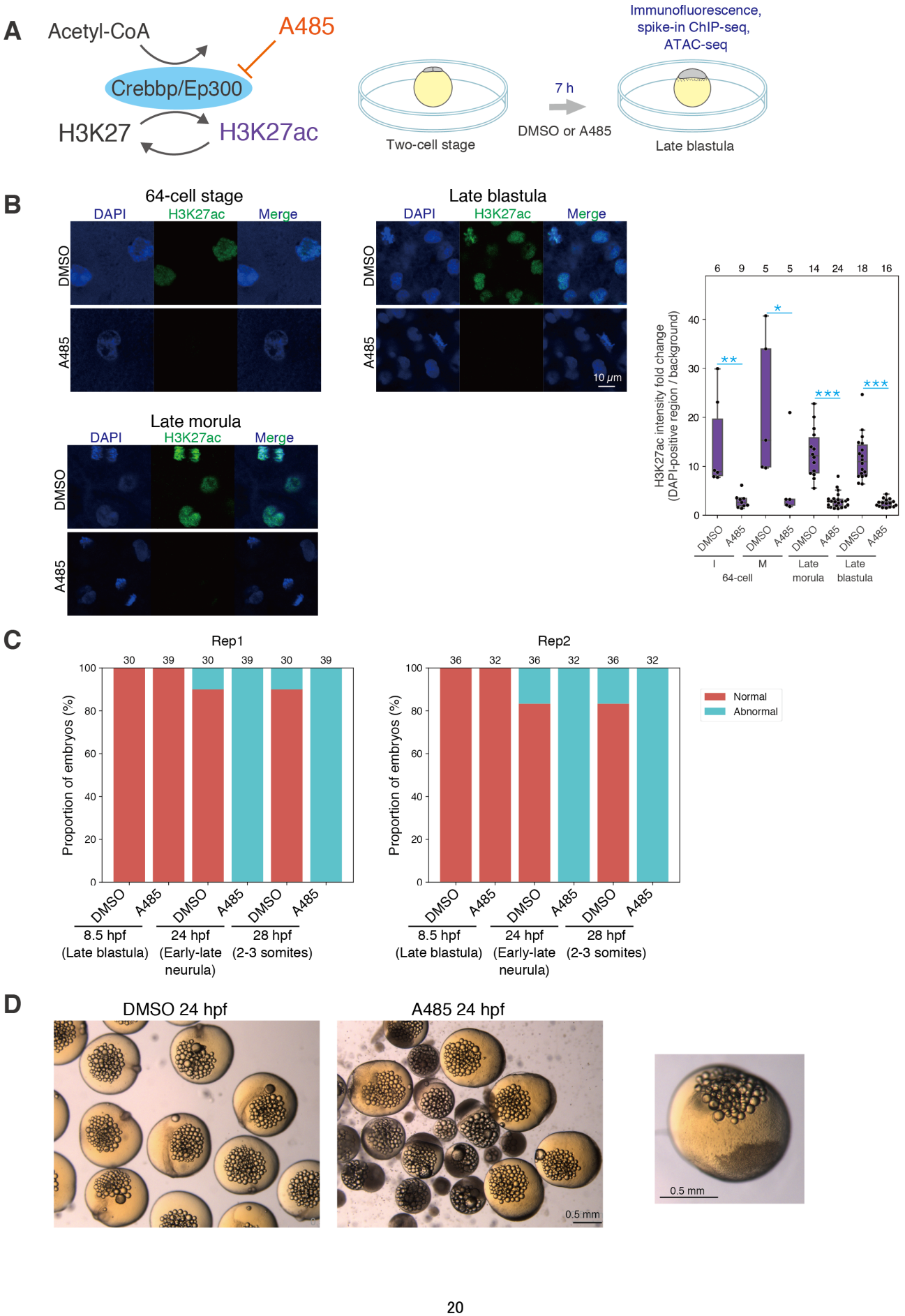
A
Acetyl-CoA
A485
Crebbp/Ep300
H3K27
H3K27ac
Immunofluorescence,
spike-in ChIP-seq,
ATAC-seq
7 h
DMSO or A485
Two-cell stage
Late blastula
B
64-cell stage
Late blastula
Late morula
DAPI
H3K27ac
Merge
DMSO
A485
10 μm
H3K27ac intensity fold change
(DAPI-positive region / background)
6 9 5 5 14 24 18 16
I
M
Late morula
Late blastula
64-cell
C
Rep1
Rep2
Proportion of embryos (%)
Normal
Abnormal
30 39 30 39 30 39
36 32 36 32 36 32
8.5 hpf
(Late blastula)
24 hpf
(Early-late
neurula)
28 hpf
(2-3 somites)
D
DMSO 24 hpf
A485 24 hpf
0.5 mm

Supplemental Figure S16. Phenotype and global change in H3K27ac accumulation after A485 treatment.
(A) Schematics of A485 experiments. Crebbp/Ep300 induces H3K27ac, and acetyl-CoA is its substrate. A485 competitively inhibits Crebbp/Ep300 catalytic activity (Lasko et al. 2017). Dechorionated embryos were incubated with DMSO or 20 μM A485 from the two-cell stage. After 7 hours of incubation, the embryos were used for immunofluorescence staining, ChIP-seq and ATAC-seq.
(B) Immunofluorescence staining of H3K27ac (left) and boxplots showing the signal intensities of each histone modification in DAPI-positive regions (right). Each dot indicates the average intensity in a single embryo. The intensity was normalized by background intensity. Phases of cell cycle after the late morula stage are not indicated because cells divide asynchronously from the late morula stage. The number above each plot indicates the number of embryos examined. Wilcoxon's rank-sum test, *** $p < 0.001$, ** $p < 0.01$, * $p < 0.05$, respectively. I: interphase, M: mitotic phase.
(C) Percentages of normal and abnormal embryos. Two biological replicates are shown separately. The number above each bar indicates the number of total embryos in each condition.
(D) Phenotypes observed at 24 hpf. Embryonic body was normally formed in DMSO-treated embryos while gastrulation arrest was observed in A485-treated embryos. The representative image of A485-treated embryos was enlarged in the panel on the right. hpf = hours post fertilization.

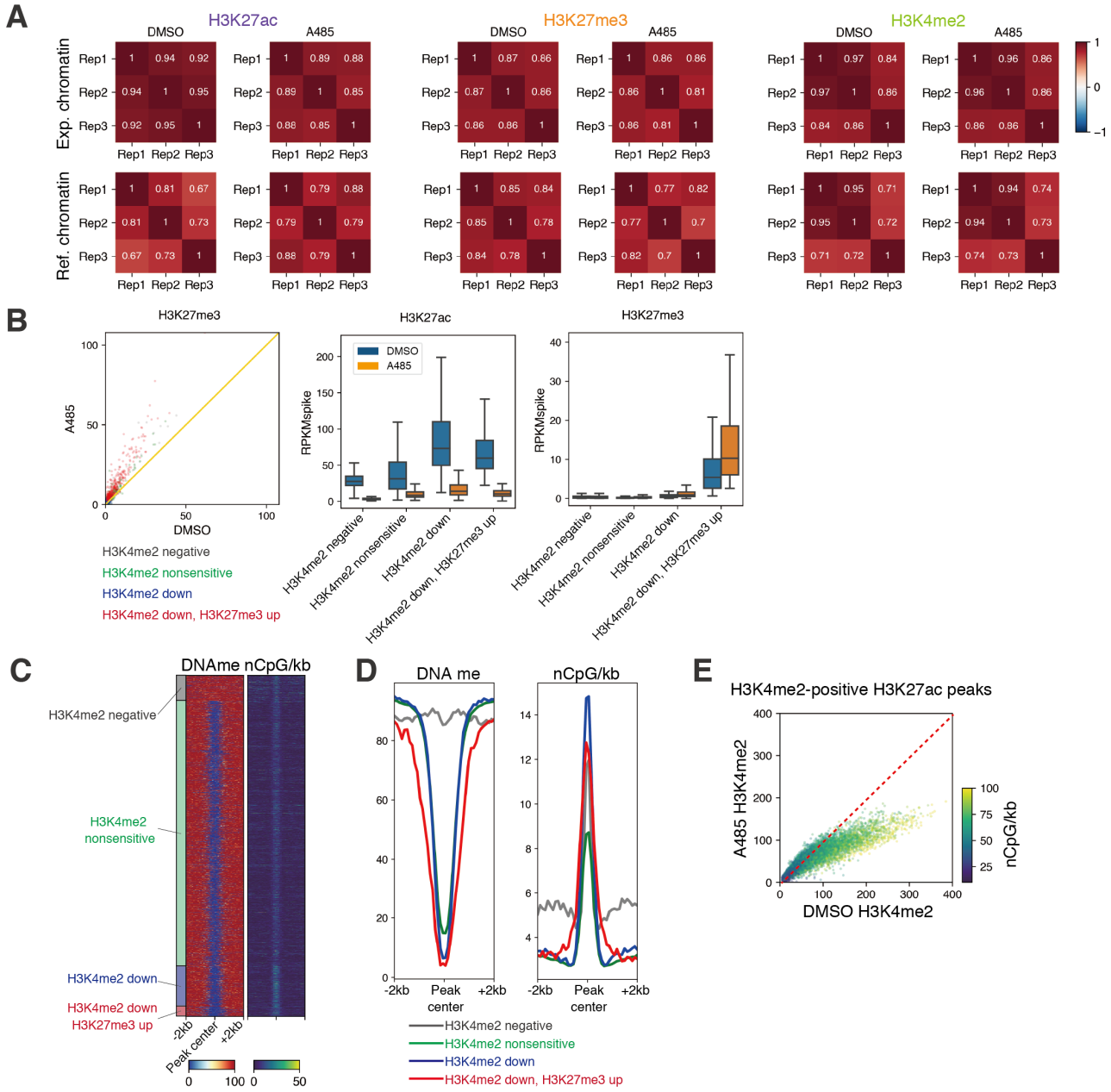

Supplemental Figure S17. Analysis of spike-in ChIP-seq data of A485-treated embryos.
(A) Heatmaps showing Pearson's correlation coefficients between two biological replicates of experimental and reference chromatin. Pearson's correlation was calculated using Log2 (RKPMspike or RPKMconv + 0.5) for each 5000 bp window-divided genomic interval (RPKMconv: conventional RPKM, RPKMspike: spike-in normalized RPKM).
(B) Scatter plot and boxplots showing H3K27ac and H3K27me3 enrichment in H3K27ac peaks in DMSO and A485 treatment. Yellow line indicates y=x.
(C, D) Heatmaps showing DNA methylation levels at the blastula stage and CpG densities (number of CpG / kb) around H3K27ac peaks (± 2 kb from peak center, window = 100 bp) (E), and line plots showing their averages in each group (F). DNA methylation data was obtained from (Qu et al. 2012).
(E) Comparison of H3K4me2 levels in DMSO or A485-treated embryos and CpG densities (number of CpG / kb) in H3K27ac peaks overlapping with H3K4me2 peaks. The red and dashed line indicates y=x.

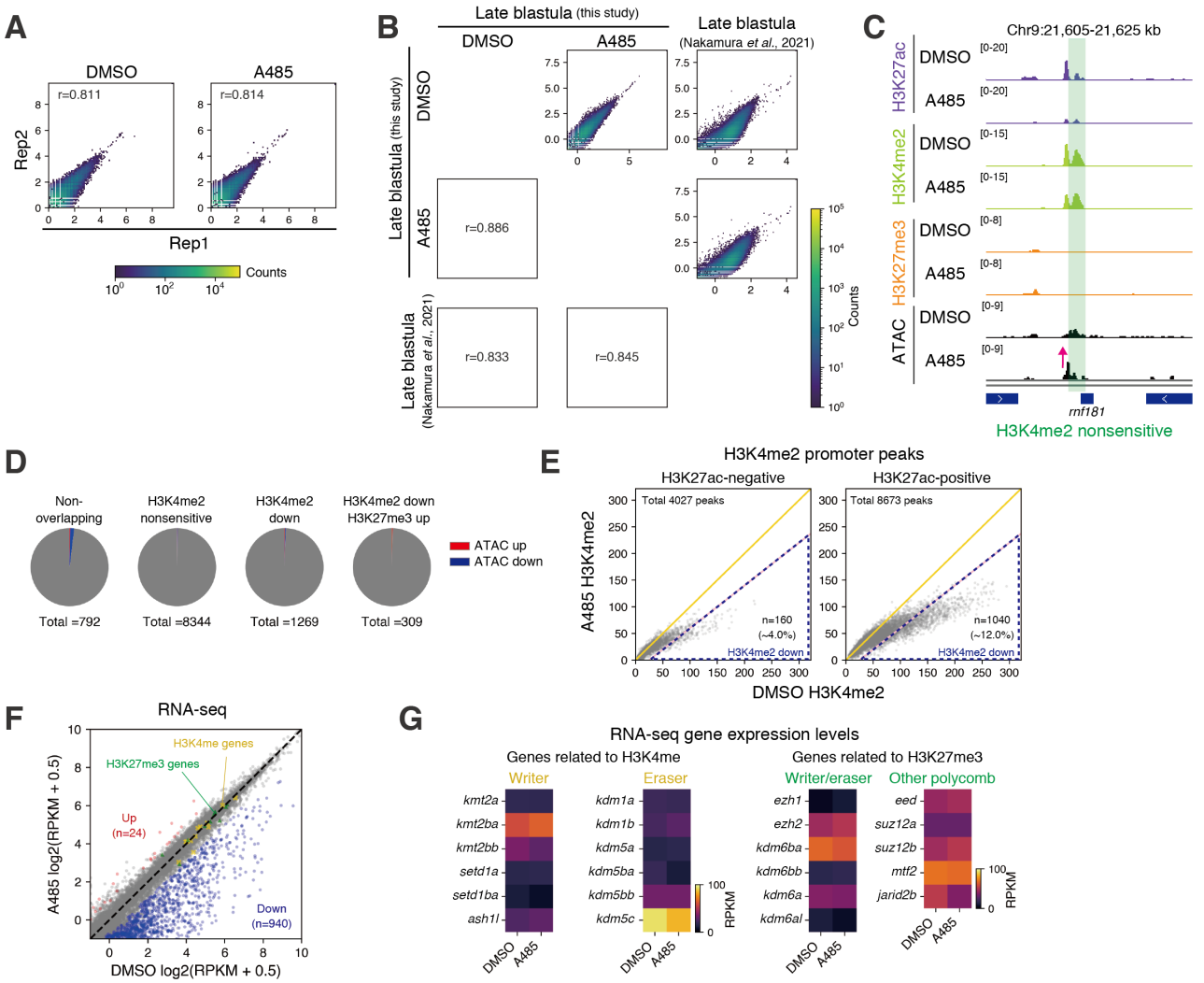

Supplemental Figure S18. Analysis of ATAC-seq data of A485-treated embryos and assessment of secondary effects of A485-treatment.

(A) 2D histograms showing correlation between two biological replicates of experimental and reference chromatin. Log2 (RPKMconv + 0.5) for each 5000 bp window-divided genomic interval and Pearson's correlation coefficients (r) are shown (RPKMconv: conventional RPKM).

(B) 2D histograms showing correlation between experiment in this study and data from a previous study (Nakamura et al. 2021). RPKMconv of pooled samples are used here. Log2 (RPKMconv + 0.5) for each 5000 bp window-divided genomic interval and Pearson's correlation coefficients (r) are shown (RPKMconv: conventional RPKM).

(C) Track view showing the histone modification enrichments after spike-in normalization and chromatin accessibility in DMSO or A485-treated embryos. The magenta arrow indicates where chromatin accessibility was altered after A485 treatment. See also in Figure 6A.

(D) Pie charts showing the proportion of H3K27ac peaks whose chromatin accessibility was reproducibly affected by A485 treatment.

(E) Scatter plots showing H3K4me2 levels in H3K27ac-negative H3K4me2 peaks (right) or H3K27ac-positive H3K4me2 peaks (left). Dots within blue and dashed were "H3K4me2 down" peaks (less than the threshold y=0.8x-20). These show that the "H3K4me2 down" peaks were mostly specific to the H3K27ac-positive H3K4me2.

(F, G) Scatter plot showing global changes in gene expression levels (F) and heatmaps showing those of representative genes (G). None of genes involved in direct deposition or erasure of H3K4 methylation and H3K27me3 were significantly altered, and their fold changes were much weaker than that of differentially expressed genes.

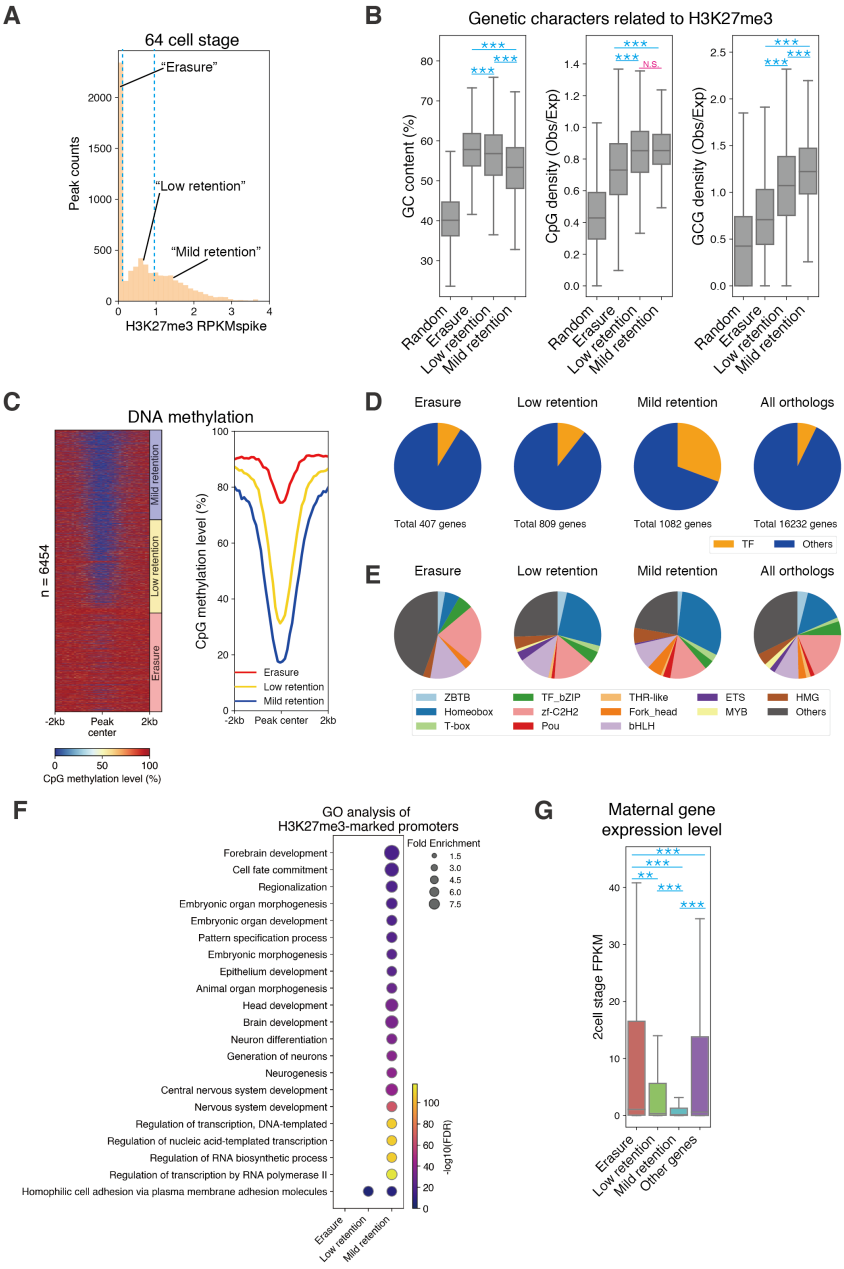

Supplemental Figure S19. Genomic regions silenced in oocytes and having high-affinity for Polycomb residually retain H3K27me3.

(A) A histogram of H3K27me3 levels after spike-in normalization (RPKMspike) in H3K27me3 merged peaks at 64 cell stage. As indicated with dashed lines, peaks were divided into three groups based on H3K27me3 RPKMspike value at the 64-cell stage ("Erasure": RPKMspike = 0, "Low retention": 0 < RPKMspike ≤ 1, "Mild retention": 1 < RPKMspike).

(B) Boxplots showing enrichment of genetic characters in each group.

(C) A heatmap showing DNA methylation levels around all H3K27me3 peaks (± 2 kb from peak center, window = 100 bp) (left) and line plot showing their averages (right). The order was sorted by RPKMspike of H3K27me3 at the 64-cell stage in heatmap. DNA methylation data was obtained from (Qu et al. 2012).

(D-E) Pie charts indicating the distribution of transcription factors (TFs) in each group (D) and pie charts showing the percentage of transcription factor family in each H3K27me3 peak group (E). Only those H3K27me3 peaks which are located at promoters and whose downstream gene have a human ortholog were included in this analysis. If several peaks are included in same promoter, the representative peaks which have highest RPKMspike value at the 64-cell stage were used. Human orthologs and human transcription factor data were obtained from Ensembl and AnimalTFDB 3.0 (Hu et al. 2019), respectively.

(F) GO terms (biological process) enriched in genes associated with H3K27me3-marked promoters. Only those GO terms with FDR less than 10^{-5} and with an enrichment of more than 3.3 fold are listed. Color indicates FDR, and circle size correlates to the fold enrichment of each GO term.

(G) Boxplots showing gene expression levels at the two-cell stage (Ichikawa et al. 2017) of genes in each group. Dwass, Steel, Critchlow and Fligner all-pairs comparison test was performed in (B and G), *** $p < 0.001$, ** $p < 0.01$, * $p < 0.05$, respectively.

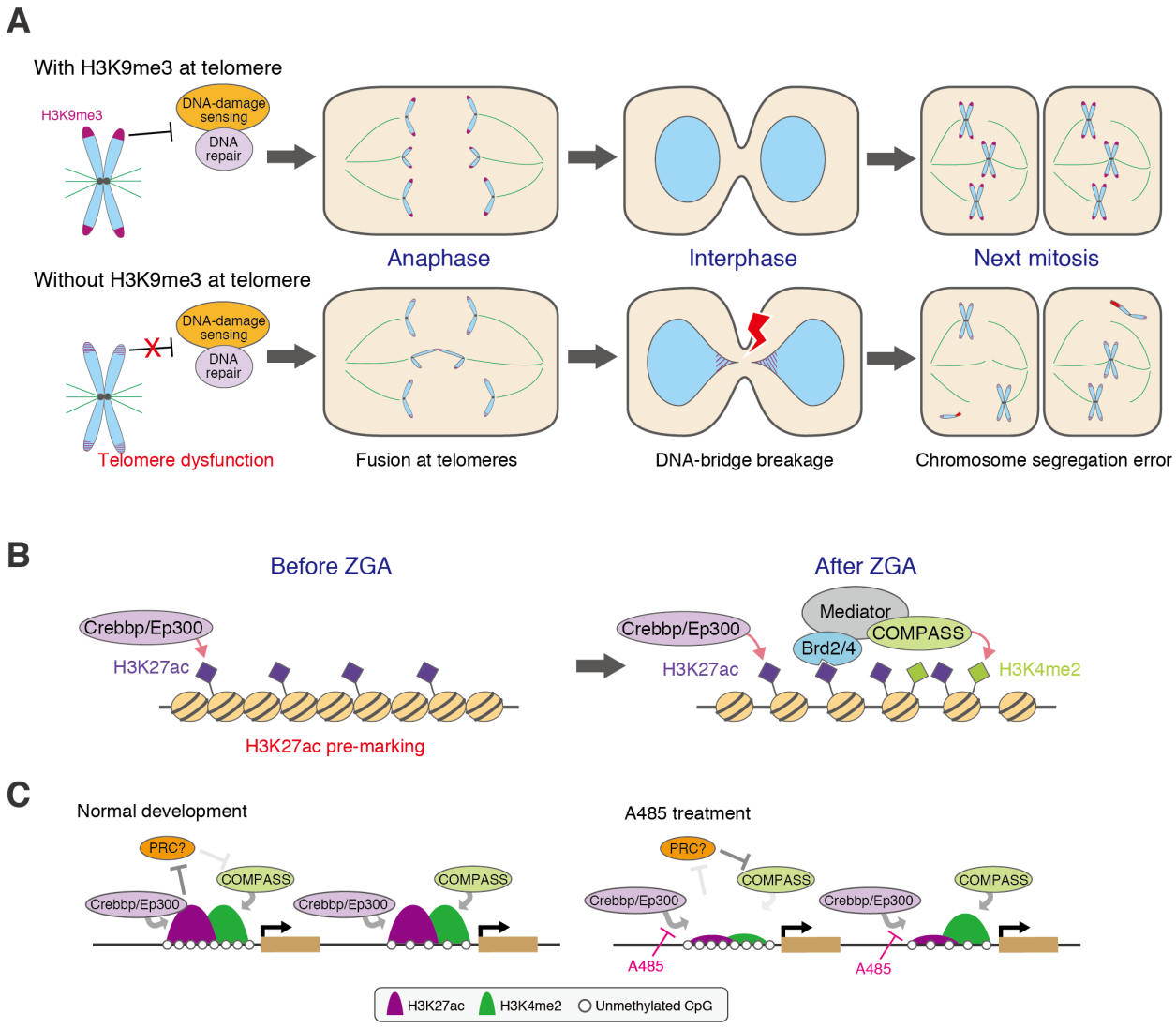

Supplemental Figure S20. Models.
(A) Schematics of residual retention of H3K9me3 at telomeric regions at early developmental stages. During early development, H3K9me3 accumulation is mainly limited to telomeric regions. Without H3K9me3 at telomeric regions, telomere dysfunction is induced and results in fusion of two chromosomes and subsequent DNA-bridge breakage, suggesting that H3K9me3 prevents telomeres from recruiting DNA-damage sensing and/or DNA repair machinery.
(B) Schematics of H3K27ac pre-marking. Crebbp/Ep300 induces H3K27ac continuously after fertilization. After ZGA, H3K27ac reader BRD2/4 or recruitment of cofactors such as mediator and COMPASS may induce H3K4me2. These genomic regions become open after ZGA, but H3K27ac is not required for this gain of chromatin accessibility.
(C) A model of modulation of H3K4me2 by Crebbp/Ep300. At CpG-dense promoters, accumulation of H3K4me2 after ZGA depends on Crebbp/Ep300-mediated acetylation, while H3K4me2 is not affected by Crebbp/Ep300 inhibition in CpG-poor promoters. Crebbp/Ep300-induced acetylation may prevent PRC1 and/or PRC2 from inhibiting COMPASS-mediated accumulation of H3K4me2 at CpG-dense promoters.

References

Hu H, Miao YR, Jia LH, Yu QY, Zhang Q, Guo AY. 2019. AnimalTFDB 3.0: A comprehensive resource for annotation and prediction of animal transcription factors. *Nucleic Acids Res* **47**: D33–D38.

Ichikawa K, Tomioka S, Suzuki Y, Nakamura R, Doi K, Yoshimura J, Kumagai M, Inoue Y, Uchida Y, Irie N, et al. 2017. Centromere evolution and CpG methylation during vertebrate speciation. *Nat Commun* **8**: 1833.

Lasko LM, Jakob CG, Edalji RP, Qiu W, Montgomery D, Digiammarino EL, Hansen TM, Risi RM, Frey R, Manaves V, et al. 2017. Discovery of a selective catalytic p300/CBP inhibitor that targets lineage-specific tumours. *Nature* **550**: 128–132.

Laue K, Rajshekar S, Courtney AJ, Lewis ZA, Goll MG. 2019. The maternal to zygotic transition regulates genome-wide heterochromatin establishment in the zebrafish embryo. *Nat Commun* **10**: 1551.

Nakamura R, Motai Y, Kumagai M, Wike CL, Nishiyama H, Nakatani Y, Durand NC, Kondo K, Kondo T, Tsukahara T, et al. 2021. CTCF looping is established during gastrulation in medaka embryos. *Genome Res* **31**: 968–980.

Nakamura R, Tsukahara T, Qu W, Ichikawa K, Otsuka T, Ogoshi K, Saito TL, Matsushima K, Sugano S, Hashimoto S, et al. 2014. Large hypomethylated domains serve as strong repressive machinery for key developmental genes in vertebrates. *Development* **141**: 2568–2580.

Qu W, Hashimoto S, Shimada A, Nakatani Y, Ichikawa K, Saito TL, Ogoshi K, Matsushima K, Suzuki Y, Sugano S, et al. 2012. Genome-wide genetic variations are highly correlated with proximal DNA methylation patterns. *Genome Res* **22**: 1419–1425.